Supporting Information

Jahn-Teller Distortion Controls Electron Transfer in Photoexcited Cu(I) Donor–Acceptor Systems

Pyosang Kim,[*,1] Xinzheng Yang,[2] Brian T. Phelan,[1] Lars Kohler,[1] Xiaosong Li,[2] Karen L. Mulfort[*,1] and Lin X. Chen[*,1,3]

[1]Chemical Sciences and Engineering Division, Argonne National Laboratory, Lemont, IL 60439

[2]Chemistry Department, University of Washington, Seattle, WA 98195

[3]Chemistry Department, Northwestern University, Evanston, IL 60208

Experimental Section.

Sample Preparation. All complexes (**1** – **4**) were synthesized and structurally characterized in the previous publication.[1]

Steady-State Measurements. Steady-state absorption spectra were measured at room temperature by Agilent Cary 60 UV-Vis spectrophotometer. Acetonitrile (MeCN) was purchased from Sigma-Aldrich and used without further purification.

Femtosecond Broadband Transient Absorption Spectroscopy. For the fs-BBTA measurements, a Yb:KGW regenerative amplifier (Light Conversion, Pharos-10W) was used to generate 1030 nm fundamental pulses at 10 kHz repetition rate with a pulse width of 160 fs. The fundamental beam was split in two pulses using 90/10 beam splitter to produce a visible pump and a broadband probe pulse. The high-power beams pumped a home-built noncollinear optical parametric amplifier (NOPA) to generate the pump pulses centered at ~ 545 nm with 55 nm bandwidth.[2] The pump pulses were compressed with a chirped mirror pair (Laser Quantum, DCM-12) and a fused silica wedge pair (Newport) to the pulse duration of 20.2 fs at the sample position, which was characterized by a second-harmonic generation frequency-resolved optical

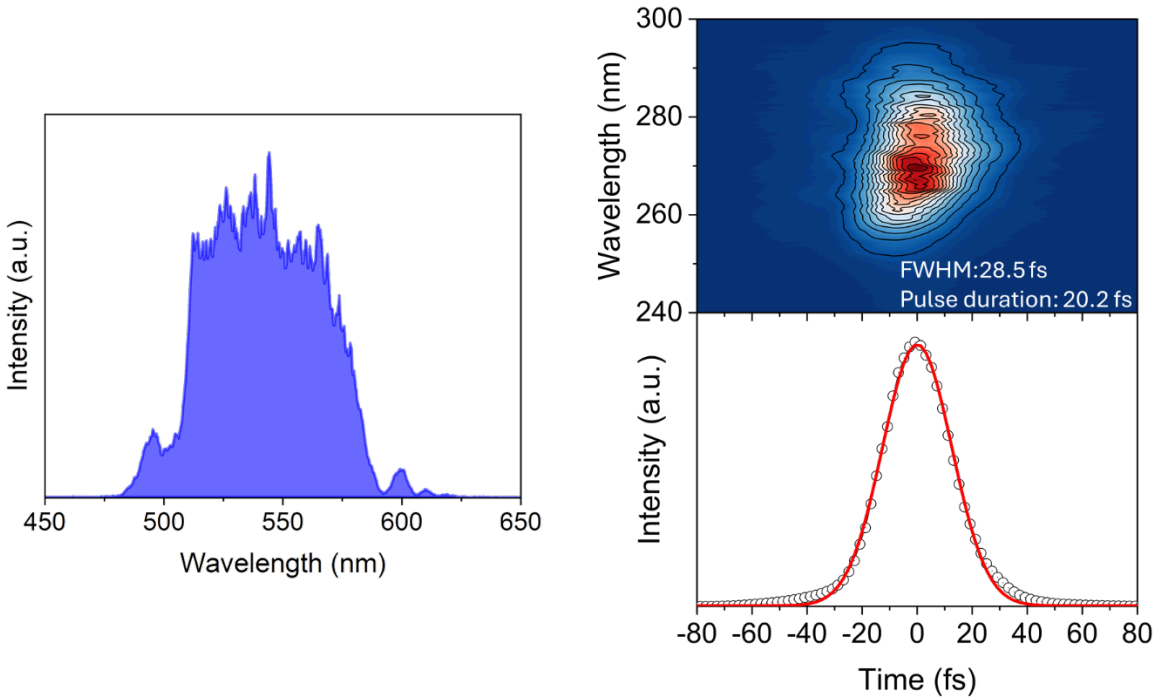

Figure S1. (Right) Pump laser pulse used for fs-BBTA measurements, and (left) the spectral and temporal profiles of the pump laser pulse obtained by the second-harmonic generation frequency-resolved optical gating (SHG-FROG). The pulse duration of 20.2 fs was characterized by fitting to a Gaussian function (red line) with 28.5 fs FWHM.

gating (SHG-FROG) with a 5 μm thick Beta Barium Borate (BBO) crystal (United Crystals Inc.) (Figure S1). For broadband probe, the low-power beams were focused on a 3 mm thick YAG window (EKSMA) by a 10 cm plano-convex lens to generate white light continuum (WLC) covering 520 – 850 nm range. The WLC was subsequently compressed by a chirped mirror pair (Laser Quantum, DCM-9). The pump and probe beams were focused on the sample contained in a 1 mm pathlength quartz cuvette using a 25 cm concave mirror. The optical time delay between pump and probe pulses was controlled by a motorized linear stage (Newport, XMS160-S). To measure the TA spectra, the "pump-on" and "pump-off" probe spectra were obtained by a chopper operating at 500 Hz and detected with a spectrometer (Andor, Kymera 328i) and a sCMOS camera (Andor, Zyla-5.5). The TA measurements were carried out with the pump polarization in a magic angle (54.7°) with respect to the probe polarization to prevent polarization-dependent signals.

Computational Methods. A development version of Gaussian quantum chemistry program package[3] was employed for all quantum chemistry calculations. The geometrical structures of the ground states of all complexes were optimized in acetonitrile (ε = 35.688) by using density functional theory (DFT)[4, 5] for the PBE0 functional[6, 7] with the Def2-TZVP (Cu atom) and Def2-SVP (H, C, N, and O atoms) all-electron basis sets.[8, 9] The SCF convergence SCF convergence requires both $1e^{-8}$ for RMS change in the density matrix and $1e^{-10}$ maximum change in the density matrix. The energy change is not used to test SCF convergence in Gaussian, but the energy change is usually smaller than $1e^{-10}$ atomic unit at converged SCF. For geometry optimization, all four criteria need to be satisfied at the same time, including maximum force < 0.00045 Hartree/Bohr, RMS force < 0.0003 Hartree/Bohr, maximum displacement < 0.0018 Bohr, and RMS displacement < 0.0012 Bohr. The D3 version of Grimme's dispersion with Becke-Johnson damping (S6=1.0000, S8=1.2177, ABJ1=0.4145, ABJ2=4.8593)[10] were added to the PBE0 functional to account for the non-covalent interactions. were added to the PBE0 functional to account for the non-covalent interactions. The solvent effect was corrected by using the integral equation formalism polarizable continuum (IEFPCM) solvation model[11] with the universal force field atomic radii. The accuracy of numerical integrations is at the ultrafine grid (99,590) level. The structures of the lowest singlet metal-to-ligand charge transfer (^{1}MLCT) and charge separated (^{1}CS) states were optimized by using the linear response time-dependent DFT (TDDFT) method[12] at the same level of theory described above. Analytical Hessian were computed to verify minima in TDDFT geometry optimizations. Vibrational frequencies are computed at the optimized geometries with harmonic approximation for vibrational mode analysis. The potential energy surfaces of the ground and excited states were obtained by

scanning the dihedral angle between two N-Cu-N planes (geometry optimizations for the ground states at a series of fixed dihedral angles with all other degrees of freedom relaxed) followed by TDDFT calculations at each ground state structure. 20 singlet and 20 triplet excited states were calculated at each optimized ground state geometry. The Douglas-Kroll-Hess 2nd order scalar relativistic correction[13-15] for two-electron integrals were applied in TDDFT calculations.

Global kinetic analysis of BBTA data. Global analysis of the BBTA data was carried out using the Glotaran software package (https://glotaran.org/), which interfaces with the R-based TIMP library for global analysis of multi-dimensional spectroscopic data.[16] Briefly, the transient absorption data matrix was globally fitted using a sum of exponential kinetic components. Singular value decomposition (SVD) was used to assess the number of significant kinetic components. Prior to global fitting, the BBTA data within the first 80 fs were truncated to eliminate contributions from the coherent spike and cross-phase modulation signals around time zero. The fitting employed a variable projection algorithm, in which the nonlinear kinetic parameters were optimized iteratively while the associated difference spectra were treated as conditionally linear parameters. In sequential model, the analysis yields the characteristic time constants and their associated evolution-associated difference spectra (EADS).

$$\Psi(\lambda, t) = \sum_{l=1}^{n_{comp}} \left[C_l^{EADS}(t, \theta)\right] \; EADS_l(\lambda)$$

where $\Psi(\lambda, t)$: measured BBTA data matrix, $EADS_l(\lambda)$: evolution-associated difference spectrum of component l, $C_l^{EADS}(t, \theta)$: sequential-model concentration profile for component l, determined by the kinetic parameters θ (lifetime τ_l). Convergence was assessed based on stabilization of the sum of squared errors (SSE) and the absence of systematic structure in the residuals.

For comparison, decay associated difference spectra (DADS) are obtained based on non-sequential model. Positive and negative DADS values represent decay and rise kinetics, respectively, at each probe wavelength for the associated time constants. In the early-time regime (up to 2.5 ps), **1** and **3** exhibit rise kinetics across the entire probe wavelength range, as evidenced by the black DADS. This behavior corresponds to the rise of the EADS (black → red EADS in Figures 1c and 1f) and is attributed to JTD. For **2** and **4**, the black DADS clearly display the spectral signature of the NDI anion with a rise component, which matches the rise dynamics of the EADS (black → red EADS in Figures 1d and 1g) and indicates PET."

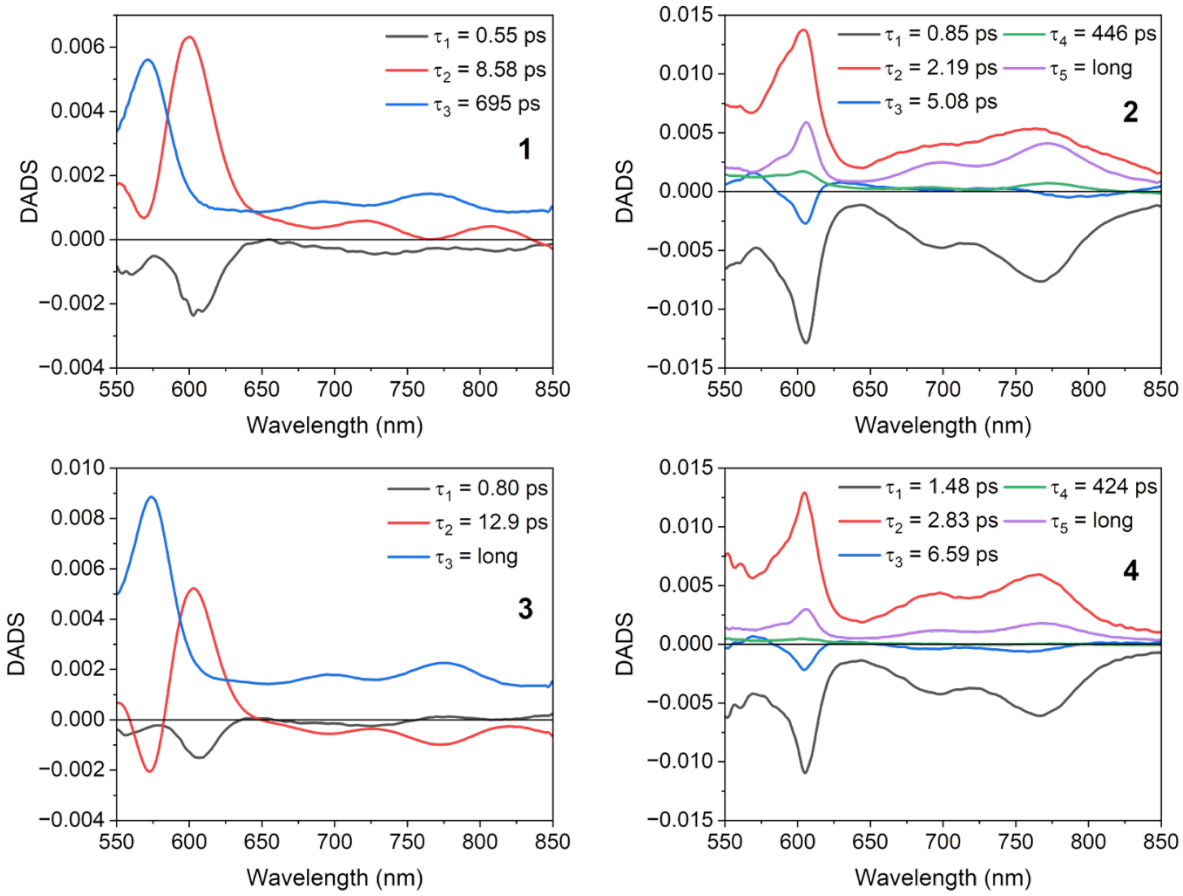

Figure S2. Decay associated difference spectra (DADS) for **1** -**4**.

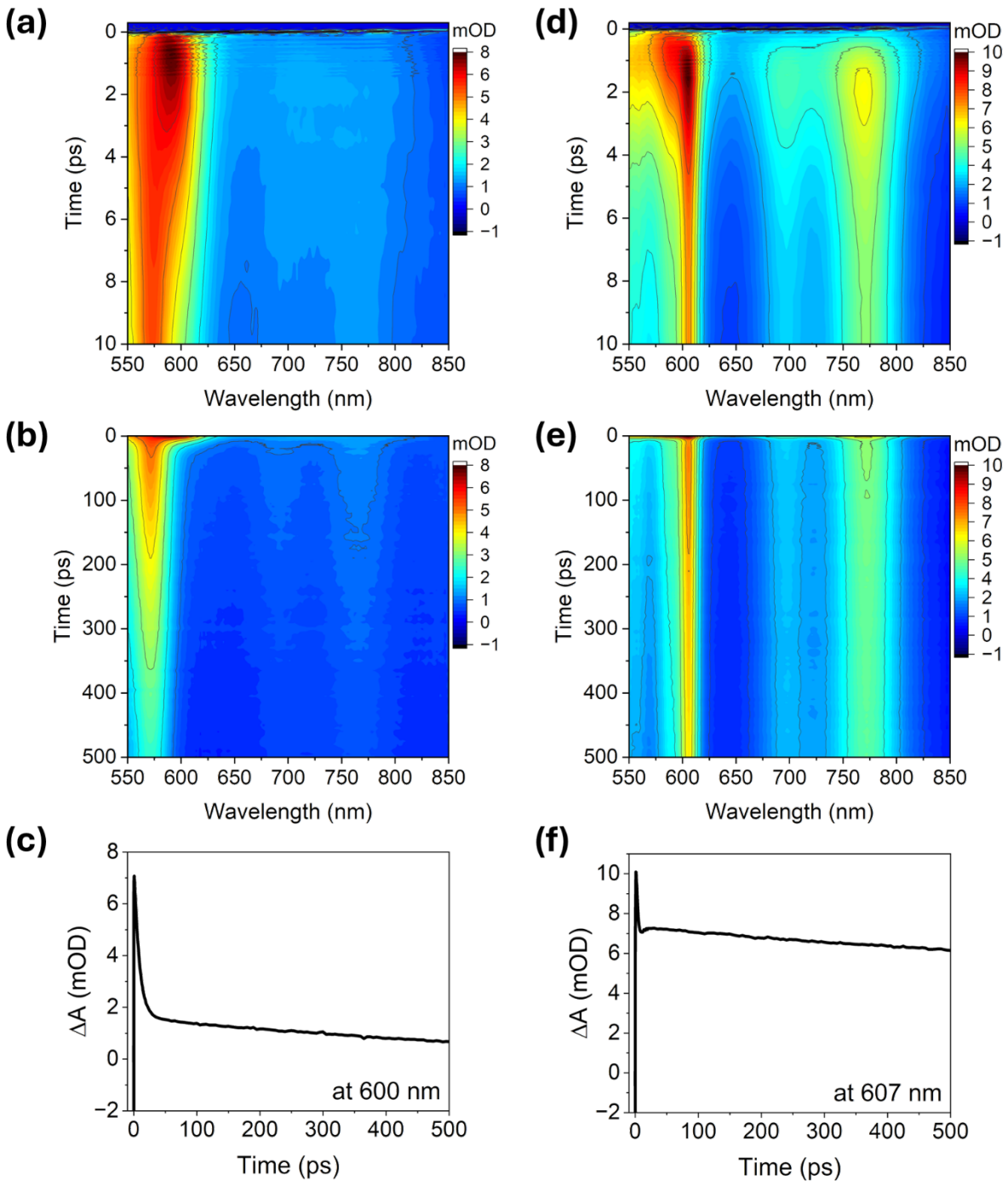

Figure S3. 2D contour plots of BBTA spectra and kinetic profiles for **1** (a,b,c) and **2** (d,e,f).

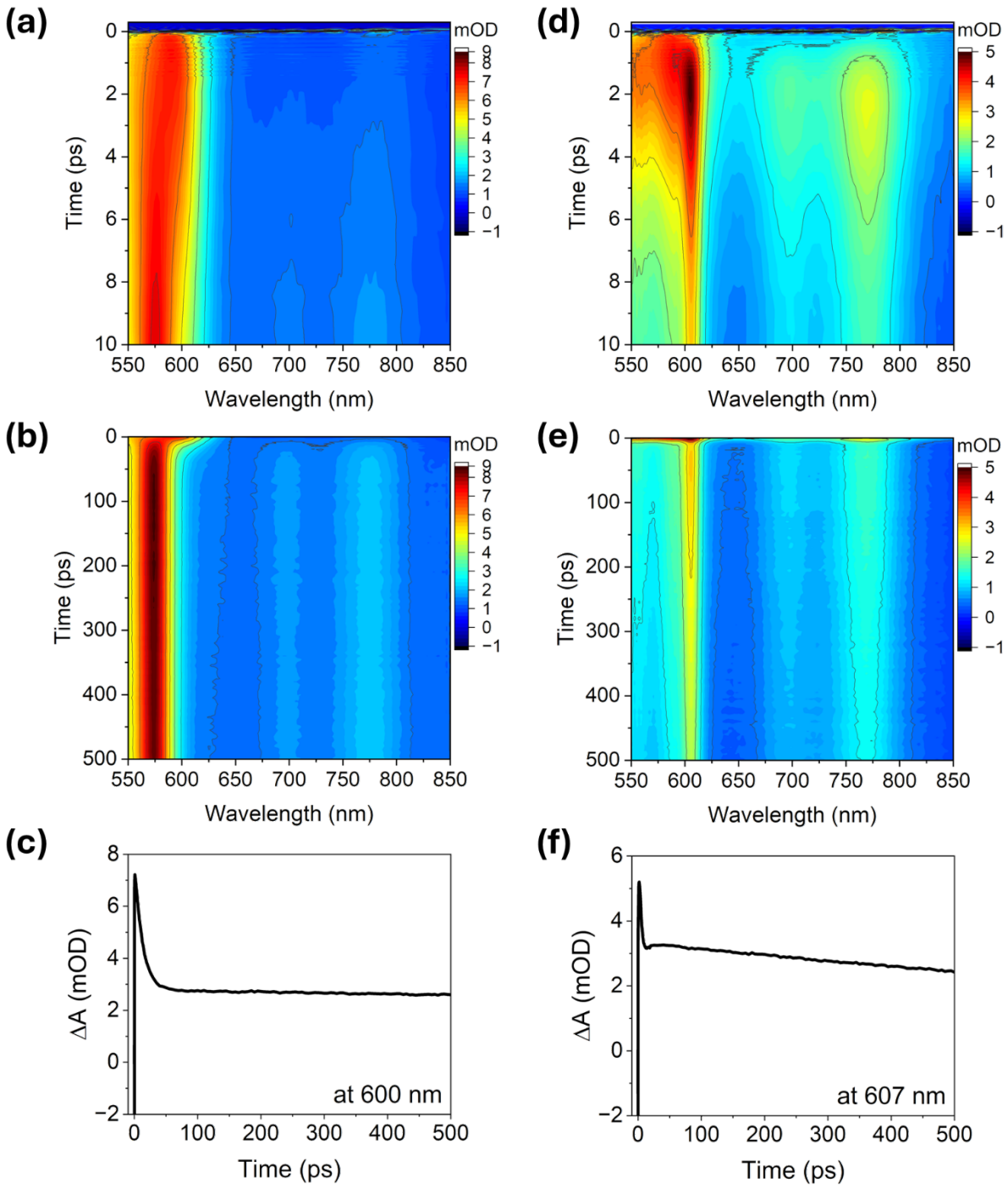

Figure S4. 2D contour plots of BBTA spectra and kinetic profiles for **3** (a,b,c) and **4** (d,e,f).

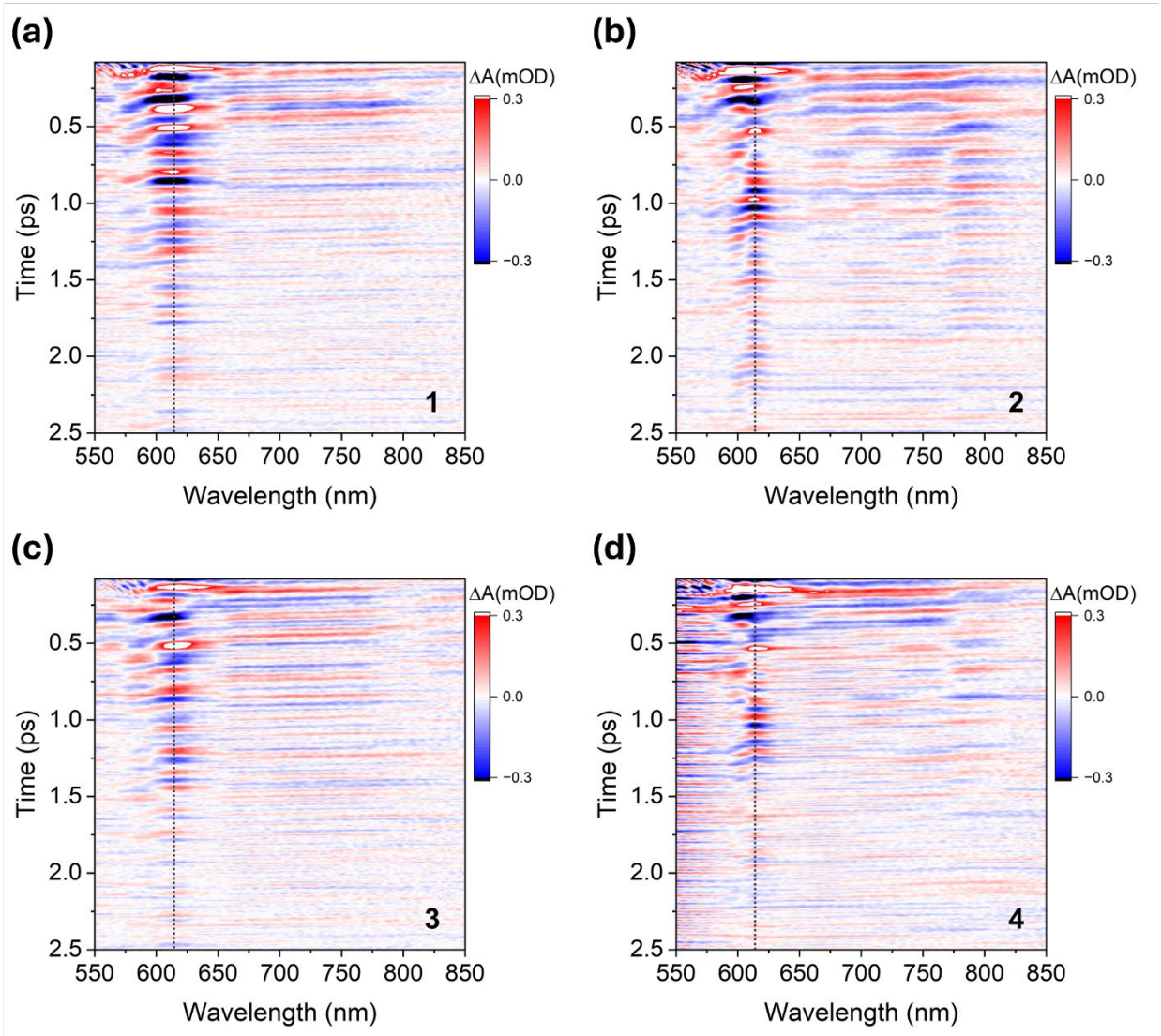

Figure S5. Oscillatory residual maps for **1**-**4**. The black dotted lines indicate the wavelength position at 615 nm.

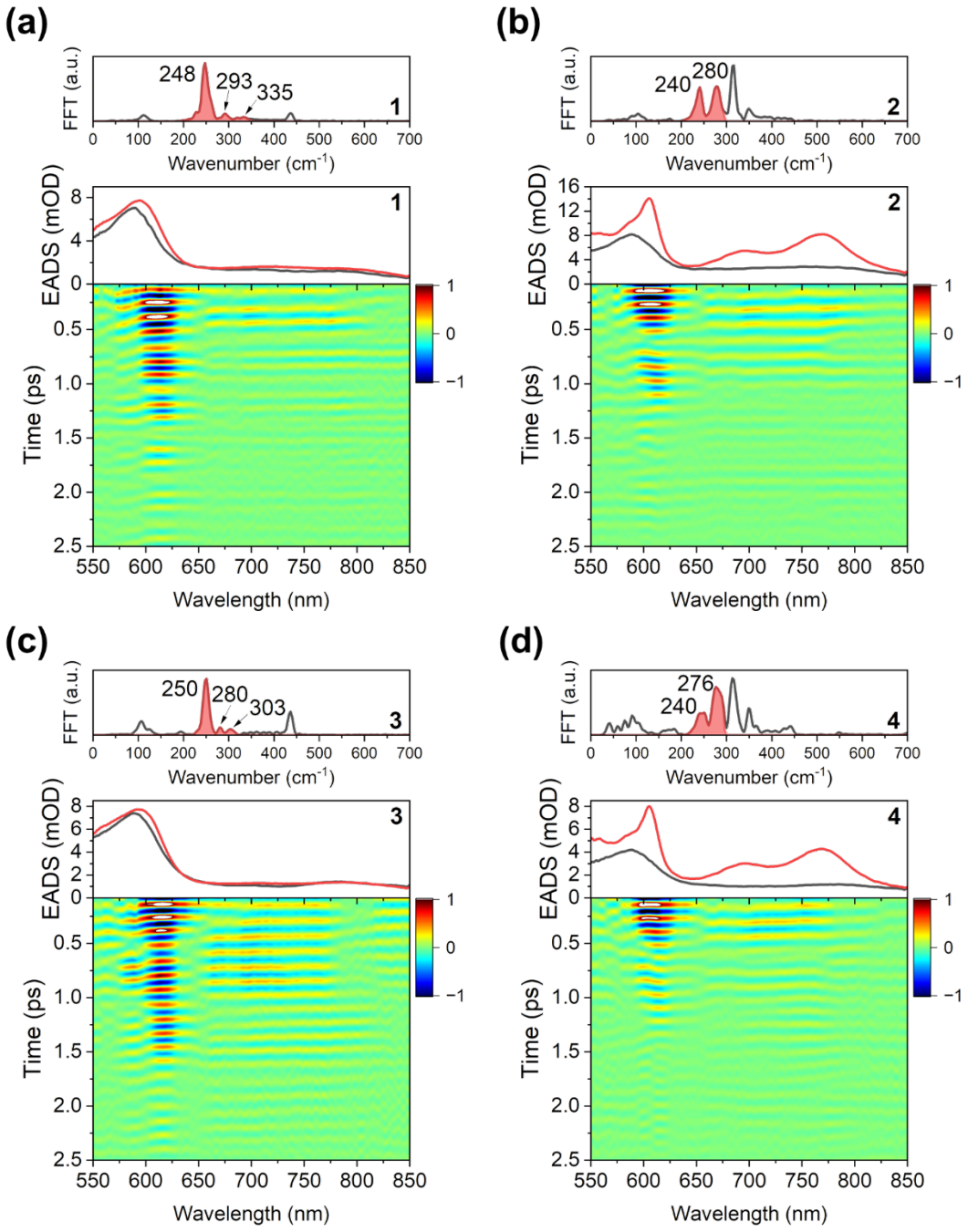

Figure S6. (a-d) Top: FFT spectra at 615 nm. The red-shaded bands indicate Fourier-filtered frequencies obtained by a super-Gaussian window. Middle: EADSs associated with JTD for **1** and **3** and PET for **2** and **4**. Bottom: Fourier-filtered oscillation maps.

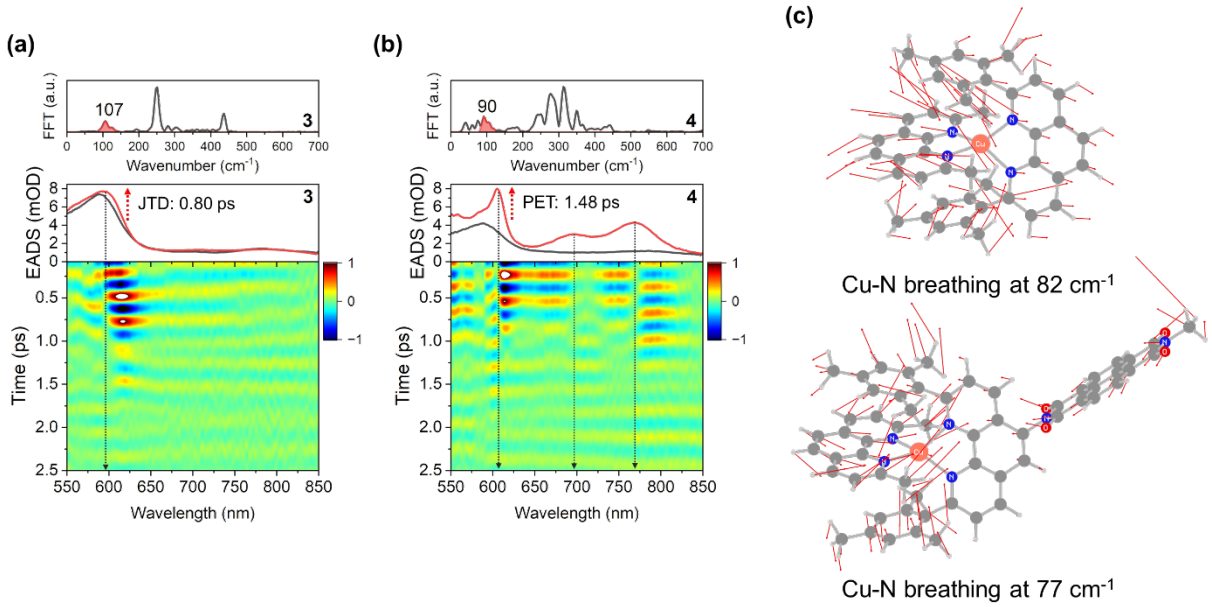

Figure S7. (a and b) Top: FFT spectra at 615 nm. The red-shaded bands indicate Fourier-filtered frequencies obtained by a super-Gaussian window. Middle: EADSs associated with JTD for **3** and PET for **4**. Bottom: Fourier-filtered oscillation maps for ~107 cm^{-1} CVWP for **3** and ~90 cm^{-1} CVWP for **4**. The dotted arrows highlight the correlation between the peak wavelengths of ^{1}MLCT ESA and NDI radical anion, and the PF wavelengths. (c) Calculated Cu-N breathing vibrations in the ground state for **3** (top) and **4** (bottom)

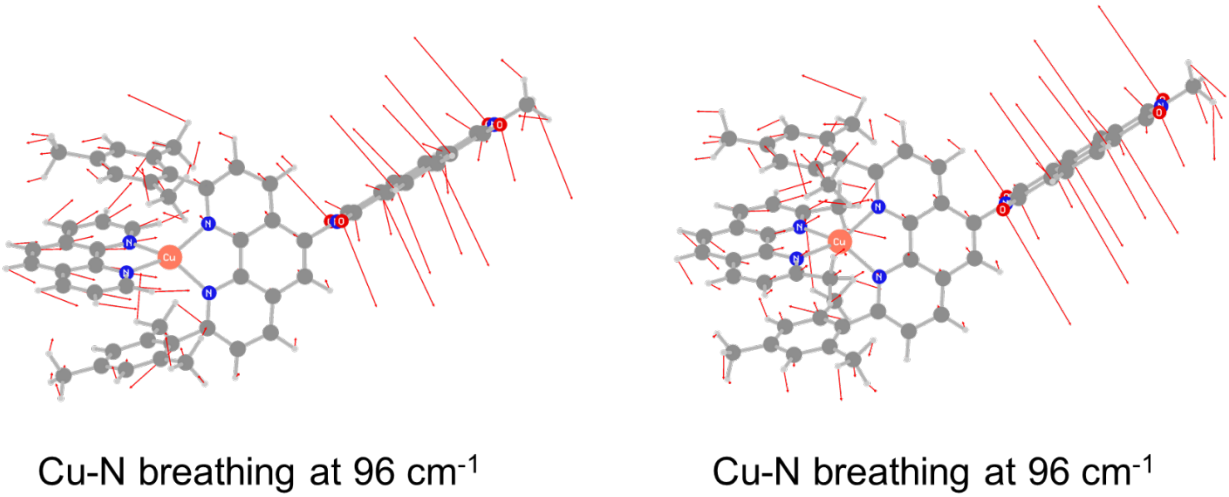

Figure S8. Calculated Cu-N breathing vibrations in the ^{1}MLCT state for **2** (left) and **4** (right)

Quantification of D-A distance modulation induced by Cu-N breathing motion. we evaluated the distance between the Cu atom and the nitrogen atom of the NDI unit linked to the mesityl-substituted phenanthroline ligand for both the contracted and expanded vibrational configurations. Specifically, based on the calculated Cu-N breathing vibrational motions, we extracted structures corresponding to the compression and elongation of the Cu–N bond within the donor (**D**) unit along the normal mode coordinate and calculated the corresponding distances between the Cu atom and the nitrogen atom of the NDI acceptor (Cu–NDI) (Figures S8 and S9). The difference between these two distances represents the structural modulation driven by the Cu–N breathing motion. In addition, we calculated the distance variation between the Cu atom and the center of the NDI acceptor. This analysis further supports that the Cu–N breathing motion can modulate the donor–acceptor separation and, consequently, the electronic coupling between the cation and anion in the DA system.

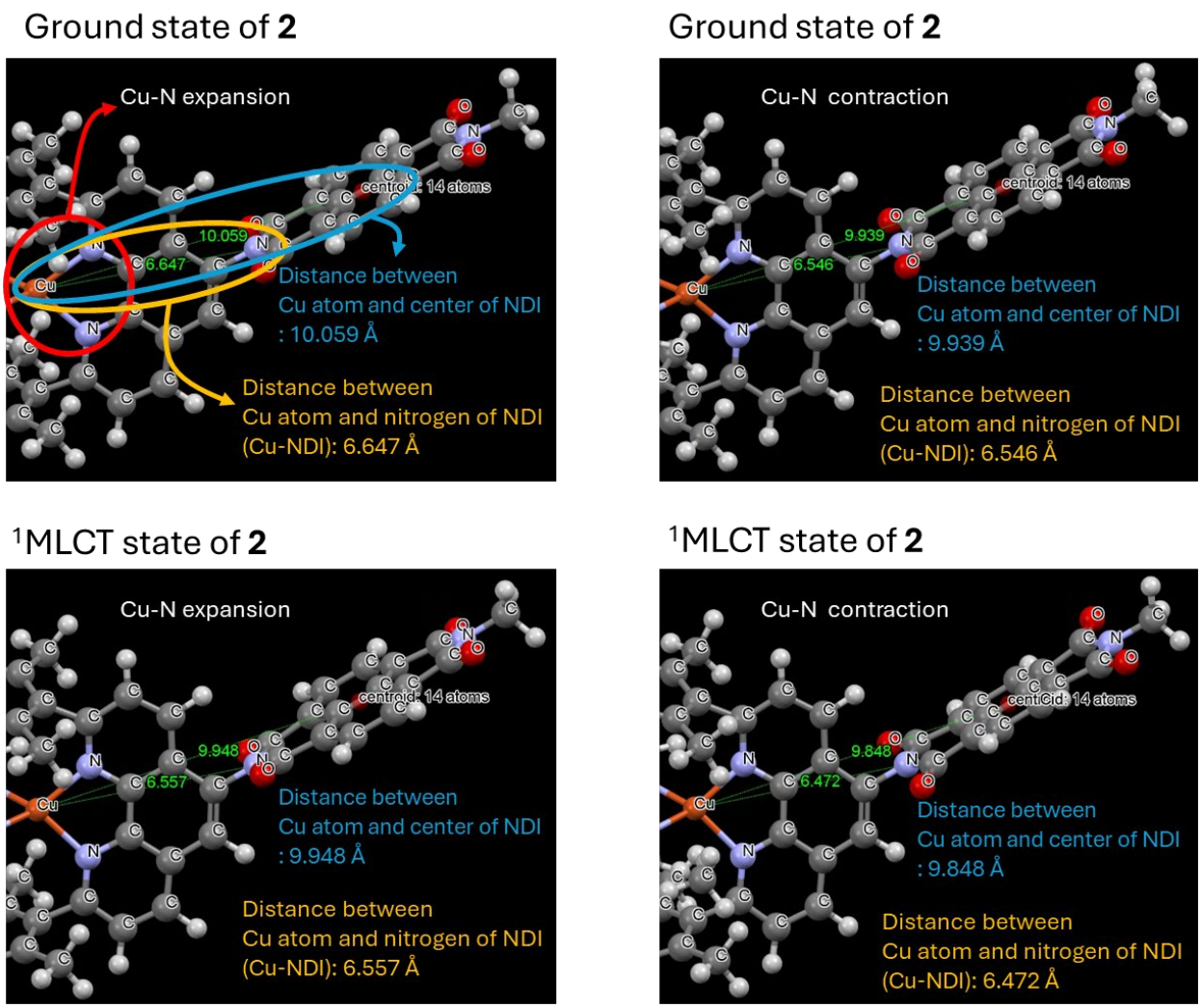

Figure S9. Calculated modulation of Cu-NDI distance induced by Cu-N breathing motion for **2** in ground state (top) and ^{1}MLCT state (bottom).

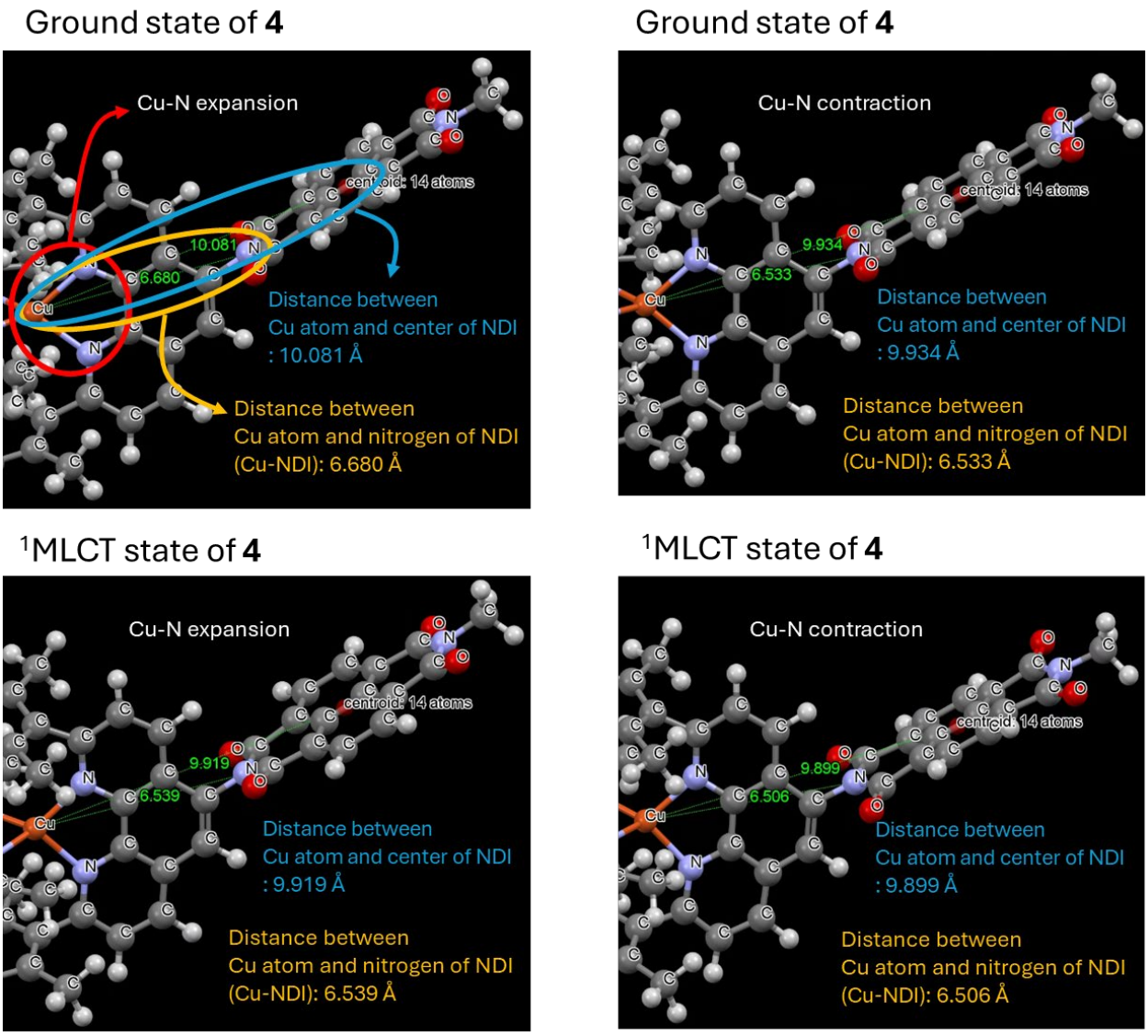

Figure S10. Calculated modulation of Cu-NDI distance induced by Cu-N breathing motion for **4** in ground state (top) and ^{1}MLCT state (bottom).

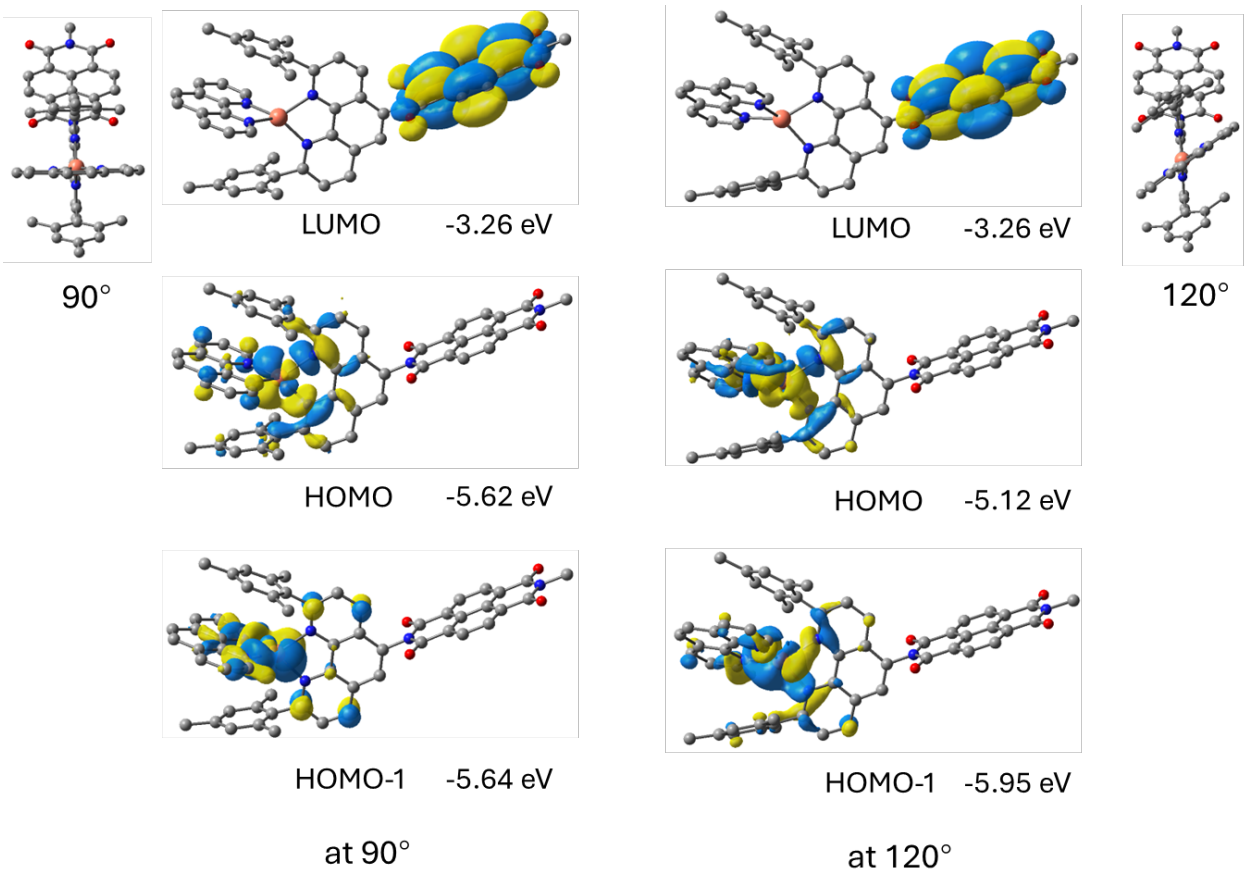

Figure S11. Frontier molecular orbitals (MOs) involved in the electronic transitions corresponding to the higher-lying CS state (HOMO−1 → LUMO) and the lowest CS state (HOMO → LUMO) for complex **2** at the dihedral angles of 90° and 120°.

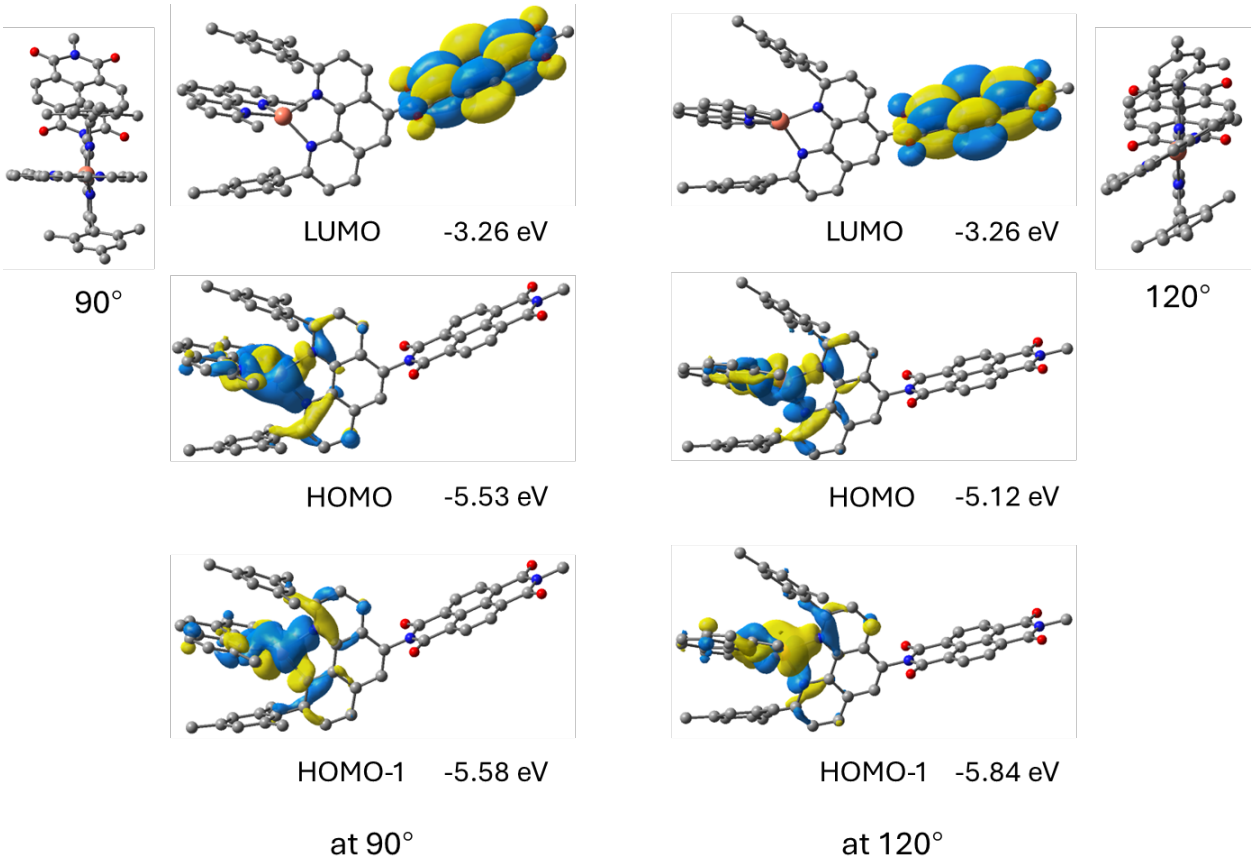

Figure S12. Frontier molecular orbitals (MOs) involved in the electronic transitions corresponding to the higher-lying CS state (HOMO−1 → LUMO) and the lowest CS state (HOMO → LUMO) for complex **4** at the dihedral angles of 90° and 120°.

References

1. D. Hayes, L. Kohler, L. X. Chen and K. L. Mulfort, *The Journal of Physical Chemistry Letters*, 2018, **9**, 2070-2076.
2. A. Grupp, A. Budweg, M. P. Fischer, J. Allerbeck, G. Soavi, A. Leitenstorfer and D. Brida, *Journal of Optics*, 2017, **20**, 014005.
3. M. J. Frisch, G. W. Trucks, H. B. Schlegel, G. E. Scuseria, M. A. Robb, J. R. Cheeseman, G. Scalmani, V. Barone, G. A. Petersson, H. Nakatsuji, X. Li, M. Caricato, A. V. Marenich, J. Bloino, B. G. Janesko, R. Gomperts, B. Mennucci, H. P. Hratchian, J. V. Ortiz, A. F. Izmaylov, J. L. Sonnenberg, Williams, F. Ding, F. Lipparini, F. Egidi, J. Goings, B. Peng, A. Petrone, T. Henderson, D. Ranasinghe, V. G. Zakrzewski, J. Gao, N. Rega, G. Zheng, W. Liang, M. Hada, M. Ehara, K. Toyota, R. Fukuda, J. Hasegawa, M. Ishida, T. Nakajima, Y. Honda, O. Kitao, H. Nakai, T. Vreven, K. Throssell, J. A. Montgomery Jr., J. E. Peralta, F. Ogliaro, M. J. Bearpark, J. J. Heyd, E. N. Brothers, K. N. Kudin, V. N. Staroverov, T. A. Keith, R. Kobayashi, J. Normand, K. Raghavachari, A. P. Rendell, J. C. Burant, S. S. Iyengar, J. Tomasi, M. Cossi, J. M. Millam, M. Klene, C. Adamo, R. Cammi, J. W. Ochterski, R. L. Martin, K. Morokuma, O. Farkas, J. B. Foresman and D. J. Fox, *Journal*, 2016.
4. P. Hohenberg and W. Kohn, *Physical Review*, 1964, **136**, B864-B871.
5. W. Kohn and L. J. Sham, *Physical Review*, 1965, **140**, A1133-A1138.
6. J. P. Perdew, K. Burke and M. Ernzerhof, *Physical Review Letters*, 1996, **77**, 3865-3868.
7. C. Adamo and V. Barone, *The Journal of Chemical Physics*, 1999, **110**, 6158-6170.
8. F. Weigend and R. Ahlrichs, *Physical Chemistry Chemical Physics*, 2005, **7**, 3297-3305.
9. F. Weigend, *Physical Chemistry Chemical Physics*, 2006, **8**, 1057-1065.
10. S. Grimme, S. Ehrlich and L. Goerigk, *Journal of Computational Chemistry*, 2011, **32**, 1456-1465.
11. J. Tomasi, B. Mennucci and R. Cammi, *Chemical Reviews*, 2005, **105**, 2999-3094.
12. E. Runge and E. K. U. Gross, *Physical Review Letters*, 1984, **52**, 997-1000.
13. M. Douglas and N. M. Kroll, *Annals of Physics*, 1974, **82**, 89-155.
14. B. A. Hess, *Physical Review A*, 1986, **33**, 3742-3748.
15. M. Barysz and A. J. Sadlej, *Journal of Molecular Structure: THEOCHEM*, 2001, **573**, 181-200.
16. J. J. Snellenburg, S. Laptenok, R. Seger, K. M. Mullen and I. H. M. van Stokkum, *Journal of Statistical Software*, 2012, **49**, 1 - 22.